Cation-Conduction Dominated Hydrogels for Durable Zinc-Iodine Batteries

Jin-Lin Yang, Tuo Xiao, Tao Xiao, Jia Li, Zehua Yu, Kang Liu, Peihua Yang, and Hong Jin Fan**

J.-L. Yang, T. Xiao, H. J. Fan
School of Physical and Mathematical Sciences
Nanyang Technological University
Singapore 637371, Singapore
E-mail: fanhj@ntu.edu.sg

T. Xiao, Z. Yu, K. Liu, P. Yang
The Institute of Technological Sciences
MOE Key Laboratory of Hydrodynamic Transients
Wuhan University, Wuhan 430072, China
E-mail: peihua.yang@whu.edu.cn

J. Li
Rolls-Royce@NTU Corporate Lab
Nanyang Technological University
Singapore, 639798 Singapore

This article has been accepted for publication and undergone full peer review but has not been through the copyediting, typesetting, pagination and proofreading process, which may lead to differences between this version and the Version of Record. Please cite this article as doi: 10.1002/adma.202313610.

Z. Yu
College of Chemistry and Molecular Sciences
Wuhan University, Wuhan 430072, China

Abstract: Zinc-iodine batteries have the potential to offer high energy-density aqueous energy storage, but their lifetime is limited by the rampant dendrite growth and the concurrent parasite side reactions on the Zn anode, as well as the shuttling of polyiodides. Herein, a cation-conduction dominated hydrogel electrolyte is designed to holistically enhance the stability of both zinc anode and iodine cathode. In this hydrogel electrolyte, anions are covalently anchored on hydrogel chains, and the major mobile ions in the electrolyte are restricted to be Zn^{2+}. Specifically, such a cation-conductive electrolyte results in a high zinc ion transference number (0.81) within the hydrogel and guides epitaxial Zn nucleation. Furthermore, the optimized Zn^{2+} solvation structure and the reconstructed hydrogen bond networks on hydrogel chains contribute to the reduced desolvation barrier and suppressed corrosion side reactions. On the iodine cathode side, the electrostatic repulsion between negative sulfonate groups and polyiodides hinders the loss of the iodine active material. This all-round electrolyte design renders zinc-iodine batteries with high reversibility, low self-discharge, and long lifespan.

1. Introduction

Conversion-type aqueous zinc batteries have garnered recognition for their cost-effectiveness, enhanced safety profile, and relatively faster kinetics in comparison to intercalation-type zinc batteries.[1-3] Owing to the high theoretical capacity (211 mAh g^{-1}), considerable redox potential (1.38 V vs. Zn/Zn^{2+}), and abundant availability in seawater (55 μg L^{-1}), iodine has been regarded as the most compatible cathode for aqueous zinc batteries.[4-6] Nevertheless, the drawbacks of aqueous zinc-iodine battery (AZIB) encompass Zn dendrites growth, hydrogen evolution reaction (HER) on Zn anode, and the shuttle effect of polyiodides.[7] During the Zn plating process, anions and Zn^{2+} migrate in opposite directions. With the progressive depletion of Zn^{2+} near the Zn metal, the salt concentration diminishes with time. According to Sand's model, when the salt concentration on the Zn anode surface reaches zero, the space charge region will produce a substantial electric field at Zn surface and triggers the uncontrolled dendrites appearance.[8-10] The critical moment at which dendrites start forming is referred to as Sand's time, as shown in **Figure 1**a and the inset equation. It can be inferred that reducing the transference number of anions (t_a) could increase the Sand's time, consequently mitigating dendritic growth.[11-12] It is noteworthy that, unlike the dense solid-electrolyte interphase formation on Li metal anode in the organic electrolyte, the anions present in commonly used Zn salts for aqueous electrolyte (e.g., $TFSI^-$, SO_4^{2-}, ClO_4^-, Cl^-) tend to generate loosely bound deprotonated hydroxyl species due to spontaneous water splitting. This phenomenon exacerbates anode corrosion.[13-14] Therefore, it is imperative to reduce the diffusible anions in aqueous electrolytes, not only to prevent dendrite formation but also to minimize the formation of undesirable byproducts.

Some pioneer strategies have been proposed to enhance the transference number of cations ($t_{\mathrm{Zn}^{2+}}$) and reduce the side effects of anions. These approaches include introducing anion acceptors to retard anions diffusion via electrostatic interactions, and physically confining anions via steric effect by using ring-shaped molecules.[15-21] Compared with the above anions-trapped methods, covalently anchoring the anions onto a stable polymeric backbone is a more efficient way to realize cation-conduction dominated electrolytes. However, solid-state electrolytes developed from Zn^{2+}-containing polymeric anions or inorganic frameworks will sacrifice the ionic conductivity due to the water-free structure and immobility of the multivalent Zn^{2+} at room temperature.[22] Till now, although the Zn^{2+} conductivity in single-ion conductors can be enhanced by increasing the molecular freedom/flexibility, the values are usually lower than 1 mS cm^{-1}.[23] In addition, the poor contact between Zn anode and solid-state electrolyte also raises the polarization and thus hinders the cell performance. As quasi-solid electrolytes for aqueous batteries, hydrogels offer a more attractive option for striking a balance between high $t_{\mathrm{Zn}^{2+}}$ and high Zn^{2+} conductivity. This is because the water-contained framework of hydrogel guarantees rapid Zn^{2+} transport, and their polymeric matrix is tailorable with various functional groups to fine-tune both chemical and physical properties.[24-27] Till now, the investigation of pure cation-conduction hydrogel is still infancy, primarily because it is challenging to avoid the introduction of extra Zn salts (e.g., $ZnSO_4$,

$Zn(OTf)_2$).[18, 28] Furthermore, constructing hydrogels with cation-dominated conduction is an enticing choice for halogen cathodes, as their ability to selectively sieve cation will eliminate the shuttle effect of soluble intermediate.

We herein design a cation-conduction dominated hydrogel (CCH), in which anions ($–SO_3^–$) are chemically bonded to the carbon chains. The as-prepared CCH delivered a notably high Zn^{2+} transference number of 0.81, which is two-fold higher than the dual-ion conductive polyacrylamide hydrogel with $ZnSO_4$ (DICH, $t_{Zn^{2+}}$=0.36). Benefiting from the strong sulfonate-Zn metal interaction, epitaxial dense Zn texture along (002) facet is observed during both Zn plating/stripping processes. The $–SO_3^–$ groups also endow the CCH with an optimized Zn^{2+} solvation structure and reconfigure the hydrogen bond networks of water molecules, thereby lowering the energy barrier associated with desolvation and mitigating surface corrosion. Additionally, the amide groups (–CONH–) near the $–SO_3^–$ ensure the smooth detachment/transport of Zn^{2+} along the hydrogel chains. As expected, the zinc symmetric cell with CCH electrolyte delivered stable voltage separation without short-circuiting over 5000 h at 1 mA $cm^{–2}$ for 1 mAh $cm^{–2}$, and over 500 h at 10 mA $cm^{–2}$ for 10 mAh $cm^{–2}$. When applied in AZIB, the electrostatic repulsion effect between $–SO_3^–$ and polyiodides ($I_3^–$, $I_5^–$, $I^–$, etc.) efficiently alleviates the detrimental shuttle effect and avert the irreversible iodine loss (Figure 1b-c). A remarkable capacity maintenance has been achieved in AZIB with an ultralow decay rate of 0.0076 ‰ per cycle after 22000 cycles at 10 C. This work provides insights to the rational design of hydrogel electrolytes for enhancing the stability of both cathode and anode in conversion-type aqueous batteries.

2. Results and discussion

The synthesis of CCH and DICH electrolytes is described in Figure S1a. In the case of CCH, protons in 2-acrylamido-2-methyl-1-propanesulfonic acid were replaced by Zn^{2+} in advance (AMP-Zn), followed by a conventional gelation process to form AMP-Zn hydrogel. As a counter, DICH comprises a typical polyacrylamide hydrogel (PAm) with the incorporation of $ZnSO_4$. The concentration of Zn^{2+} was consistently maintained at 2 M for both CCH and DICH. In contrast to the neutral PAm chains in DICH, CCH with no free anions affords distinct transport channels only for Zn^{2+}, ensuring the stable and uniform anions concentration in the bulk electrolyte (Figure S1b-c). The digital images demonstrate the similar transparency of as-prepared CCH and DICH (Figure S2). The freeze-dried CCH exhibits a continuous 3D crosslinked homogeneous porous structure (Figure 1d). From the Fourier-transform infrared (FTIR) spectroscopy analysis, two prominent vibrations at approximately 3350 and 1640 cm^{-1} are assigned to the stretching vibration of $-NH_2$ and C=O, respectively. In CCH, two obvious peaks locate at 1170 and 1038 cm^{-1} stand for the anchored sulfonate groups on AMP-Zn chains (Figure 1e).[29-30] The successful incorporation of $-SO_3^-$ in CCH was further confirmed by the covalent C–S bond and $Zn-SO_3^-$ interaction in X-ray photoelectron spectroscopy (XPS) spectra (Figure S3).

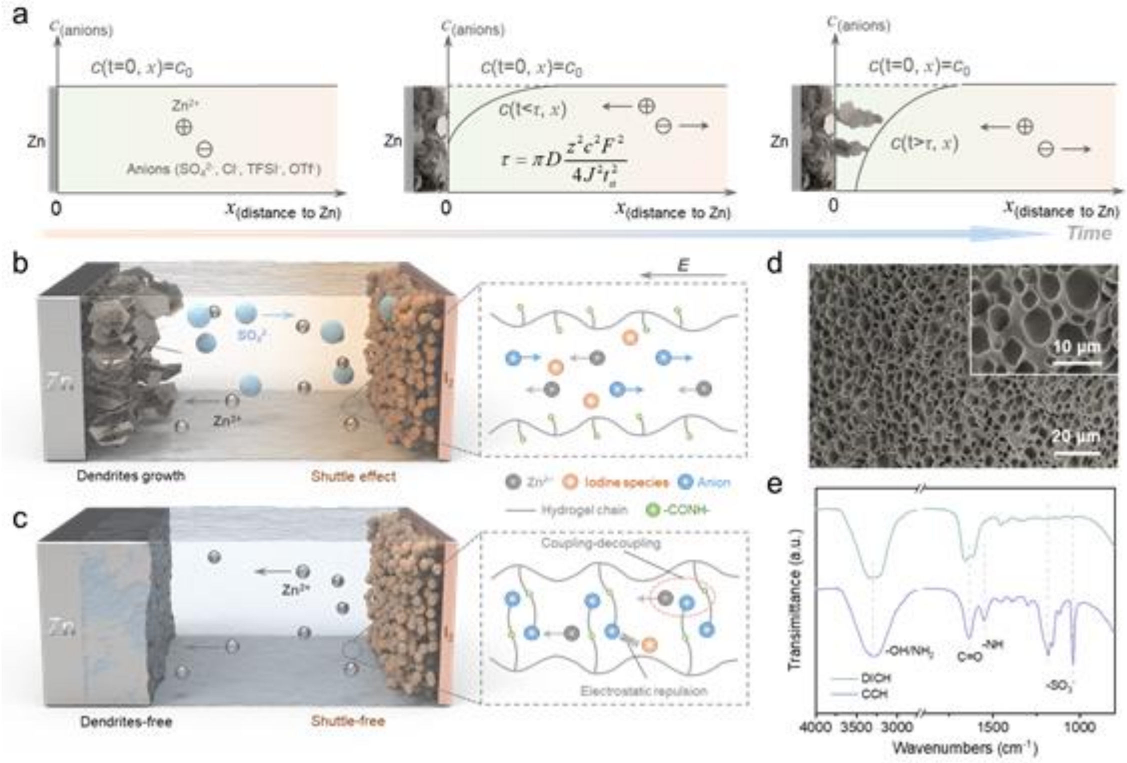

Figure 1. Fundamental function of the CCH electrolyte. (a) Theoretical interpretation of the dendrite growth of Zn electrodeposition during concentration polarization. Inset is the equation of Sand time τ: z is the charge number of the cation, D represents the ambipolar diffusion constant, J is the current density, c is the initial concentration of cations, F is the Faraday's constant, and t_a stands for the anion transference number. (b, c) Schematics of the AZIB working process and ions transport with (b) DICH and (c) CCH electrolytes. (d) SEM images of CCH after freeze-drying. (e) FTIR spectra of DICH and CCH.

The mechanical properties of the hydrogel electrolytes were subsequently evaluated. The tensile strength of CCH reaches over 36 kPa at a tensile strain over 350 %, which is more than twice the corresponding value for DICH (14 kPa) (Figure S4a). The enhanced ductility is attributed to the presence of the longer branch chains in AMP than that in PAm, which could further facilitate the accommodation of volume fluctuations in the electrodes during the charge/discharge process.[31] Furthermore, CCH delivers a strong interfacial contact with Zn anode (Figure S4b), yielding an adhesion shear strength exceeding 34.9 kPa, which is more than sixfold greater than that of DICH (5.5 kPa). Digital photos illustrating the peeling processes of DICH and CCH on Zn plates reveal a tougher bonding between CCH and Zn (Figure S4c). Correspondingly, no micro-cracks are detected at CCH-Zn interface from the cross-sectional SEM images (Figure S4d). The firm bonding between CCH and Zn was further proved by density functional theory (DFT) simulation (Figure S4e and S5). These results reveal a stronger charge transfer phenomenon occurring at the CCH-Zn interface compared to that of DICH-Zn, featuring higher adsorption energies on Zn substrates. The formation of a well-bonded hydrogel-Zn interface is crucial for dendrites inhibition. This compact interface constrains the 2D diffusion of absorbed Zn^{2+} while facilitating the creation of multiple nucleation.[32-33]

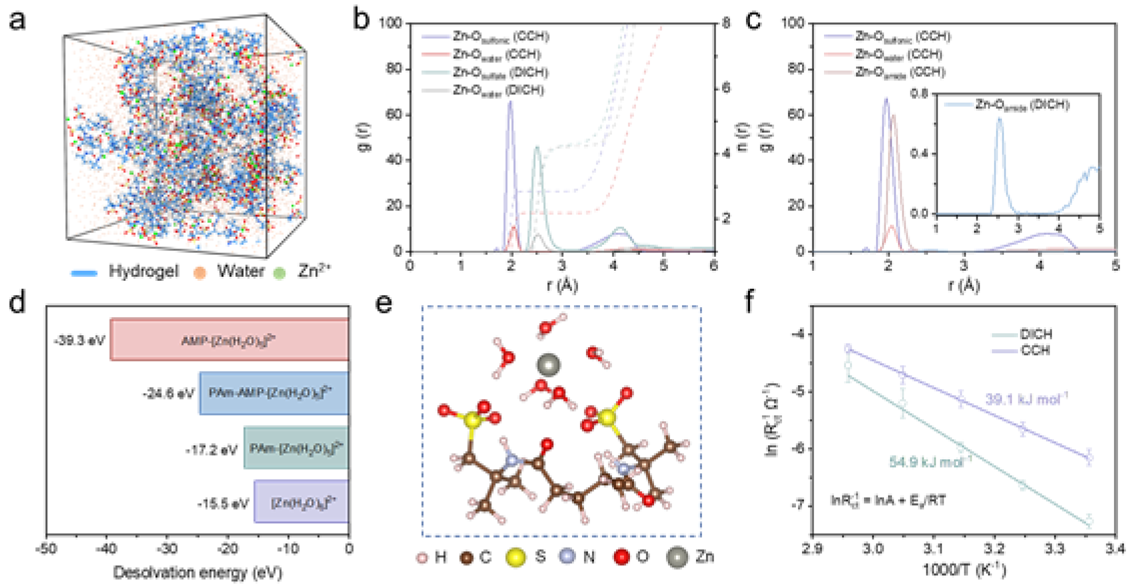

Figure 2. Solvation structure of zinc ions in CCH. (a) Molecular configuration of CCH in molecular dynamic simulations. (b) Radial distribution functions for Zn^{2+}–O collected in CCH and DICH. (c) Radial distribution functions for Zn^{2+}–O on water, amide and sulfonate groups in CCH. (d) Calculated desolvation energies of different solvation structures. (e) Simulated molecular configuration of AMP–$[Zn(H_2O)_5]^{2+}$ in CCH. (f) Arrhenius curves and activation energies in different hydrogels.

To investigate the cation-dominated conductivity function, we assessed the $t_{\mathrm{Zn}^{2+}}$ using the Bruce-Vincent method. PAm-AMPH was also fabricated for comparison (Figure S6), where half of the Zn^{2+} was provided by $ZnSO_4$, and another half was from AMP-Zn. The $t_{\mathrm{Zn}^{2+}}$ of CCH was determined to be 0.81, surpassing the values obtained for PAm-AMPH (0.59) and DICH (0.36) (Figure S7). This outcome indicates that Zn^{2+} ions are the major mobile ions in CCH. Meanwhile, CCH presents a considerable ionic conductivity (9.7 mS cm^{-1}) (Figure S8). To dive into the microscale characteristics of the hydrogel, molecular dynamics (MD) simulations were carried out (**Figure 2**a and Figure S9). By analyzing the radial distribution functions (RDFs) and coordination number (Figure 2b), we found that the bond length of Zn–O_{sulfonic} (O in $–SO_3^-$) in CCH is around 1.98 Å, which is close to the position of Zn–O_{water} (2.05 Å). This observation suggests the insertion of $–SO_3^-$ into the primary solvation shell (PSS) of Zn^{2+}.[34-36] The same peak locations of the Zn–O_{sulfate} (O in SO_4^{2-}) and Zn–O_{water} in DICH imply the existence of SO_4^{2-} in the PSS of Zn^{2+}. Besides, the g(r) value of Zn–O_{sulfonic} (~65) exceeds that for Zn^{2+}–O_{sulfate} (~47), indicating the pronounced zincophilicity of $–SO_3^-$. This value is significantly lower than that reported for sulfonic acid-modified covalent organic frameworks (~160).[28] This difference may be attributed to the solvation effect of CCH chains with amide groups, suggesting that Zn^{2+} is more likely to be stabilized in the location between amide and sulfonate groups (Figure 2c). Hence, the Zn^{2+} will dissociate easily rather than being entrapped by $–SO_3^-$.[37] In contrast, due to the limited effect of amide groups on Zn^{2+} hydration structure (inset of Figure 2c), the DICH hydrogel chain slightly influences the Zn^{2+} transport.

As observed in Figure 2d-e and Figure S10, the Zn^{2+} solvation structure optimization in CCH is attained by AMP–$[Zn(H_2O)_5]^{2+}$ with the most negative desolvation energy at approximately –39.3 eV, indicating that CCH is more promising to remove the water shell of Zn^{2+} compared with DICH and PAm-AMPH.[38] Such verdict is corroborated by the distribution of relaxation times (DRT) analysis (Figure S11), wherein the resistance of Zn^{2+} desolvation process is sharply reduced in CCH. As a result, the lowest active energy (E_a) of the symmetric cell with CCH, as calculated using the Arrhenius equation (Figure 2f and Figure S12), signifies the improved interfacial kinetics in CCH for Zn^{2+} plating.[39-40]

In addition to the optimization of hydrated Zn^{2+}, hydrogel chains also influence the state of water, as the oxygen/nitrogen-containing groups interact with H_2O. As summarized in **Figure 3**a and Figure S13, O atoms in $–SO_3^–$ groups form a greater number of hydrogen bonds (H-bonds) compared to O and N in amide groups. In DICH, H-bonds originating from amide groups are the dominant, and it is notable that these H-bonds exhibit weaker strength, as evidenced by longer bond distance, than those involving $–SO_3^–$ groups.[41] The formation of H-bonds in CCH is further substantiated by the positive shift of the ^1H peak in the nuclear magnetic resonance (NMR) spectra (from 4.673 ppm in 2 M $ZnSO_4$ solution to 4.683 ppm in AMP-Zn), as shown in Figure S14a. Correspondingly, the TG analysis shows a sluggish water loss in CCH with the increase of temperature (Figure S14b), further attesting the robust hydrogen bond interactions. Raman spectra analysis reveals a blue shift of the v-$SO_4^{2–}$ band from 973.6 to 981.9 $cm^{–1}$ in DICH and PAm-AMPH (Figure S15a-b). This shift indicates a heightened inclination of $SO_4^{2–}$ to engage in the Zn^{2+} solvation sheath, thereby forming solvent separated ion pair upon the introduction of hydrogel frameworks, in accordance with the RDFs results (Figure 2b).[42] In contrast, CCH presents no signals of v-$SO_4^{2–}$, while the symmetric vibrations of $–SO_3^–$ (1035 $cm^{–1}$) and Zn^{2+}-$^–OSO_2$-R (300 $cm^{–1}$) are well distinguished (Figure S15c).[43]

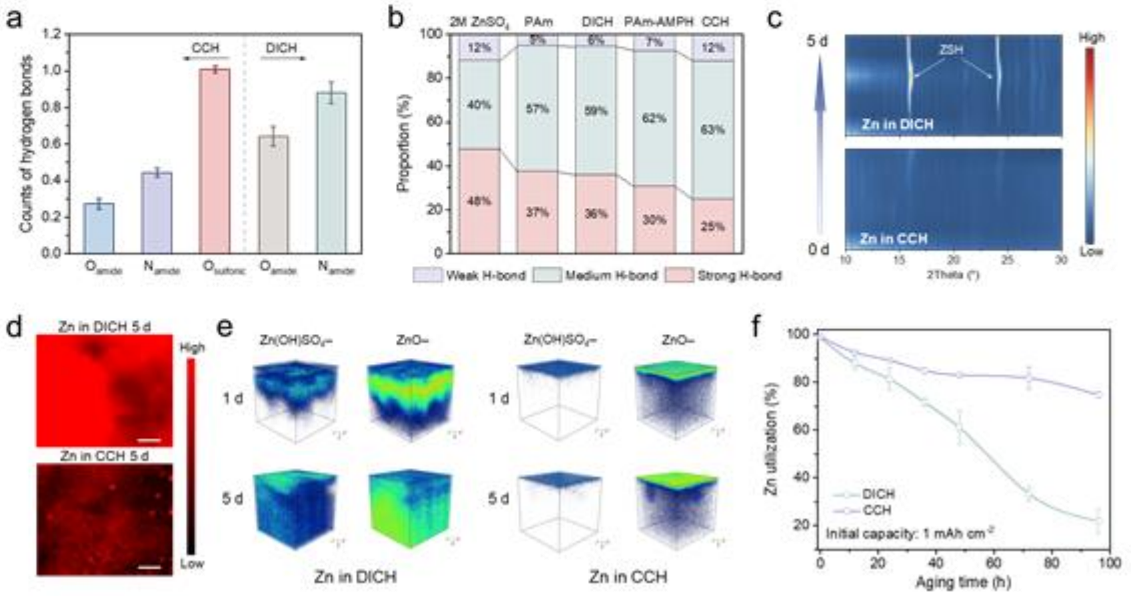

Figure 3. Water activity in CCH and anti-corrosion effect investigation. (a) Counts of the hydrogen bonds in DICH and CCH. (b) Proportions of strong, mediate, and weak hydrogen bonds in different electrolytes based on the Raman spectra analysis. (c) Ex-situ XRD contours, (d) 2D Raman mappings

(at 974 cm^{-1}) (Scale bar: 1 μm), (e) ToF-SIMS depth profiles, and (f) post-aging reversibility tests with Zn electrodes in CCH and DICH.

To unveil the water activity in different hydrogels, the composition of the peak associated with OH^- stretching vibration (3000-3700 cm^{-1}) was analyzed (Figure 3b and Figure S15d). The probability of strong H-bonds decreases with the incorporation of hydrogel, dropping from 48 % (2 M $ZnSO_4$) to 36% (DICH), illuminating the disruption of H-bonds between free H_2O molecules induced by $-NH_2$ and C=O groups on PAm. In CCH, the proportion of strong H-bonds further diminishes to 25 %. This substantial reduction in strong H-bonds endorses that $-SO_3^-$ in CCH are effective in curtailing water activity by re-establishing H-bond networks.[44-45] The fundamental mechanism underlying the solvation structure optimization in CCH and reconstruction of solvent H-bonds can be elucidated based on the Flory theory.[46-47] According to this theory, densely packed molecules (polymeric hydrogel chain) replace H_2O in PSS with zincophilic centers, weakening the hydration effect. Simultaneously, the outer water molecules are confined by H-bonds along the hydrogel chain. Consequently, the presence of free H_2O molecules is greatly reduced or even eliminated.

The HER activity was assessed by individually covering DICH and CCH on Zn plates, followed by a resting period from 0 to 5 days. Subsequently, we recorded the corresponding X-ray diffraction (XRD) patterns. As illustrated in Figure 3c and Figure S16, the intensity of the diffraction peaks corresponding to $Zn(OH)_6SO_4{\bullet}5H_2O$ (ZSH) on the Zn plate in contact with DICH increases with prolonged resting time. In contrast, no corresponding peaks are found on the Zn plate attached to CCH. Raman mapping of the peak representative of ZSH at 970 cm^{-1} also implies the negligible ZSH content on Zn in CCH (5 μm ×5 μm area, Figure 3d). The retarded HER corrosion in CCH is evidenced by the surface morphology as well, where the Zn plate remains in its original smooth state, while the one in DICH is overwhelmed by irregular ZSH sheets (Figure S17). Above results are substantiated by additional analyses, including XPS spectra, linear sweep voltammetry (LSV) tests, and Tafel plots (Figure S18).

To scrutinize the evolution of the surface passivation with increasing resting time, Time-of-Flight secondary ion mass spectrometry (ToF-SIMS) was implemented to reveal the surface composition (Figure 3e and Figure S19). By comparing the distribution of ZnO– and Zn(OH)SO_4– species on Zn plates at different time points, we can see that the ZSH layer formed in DICH electrolyte gradually thickens with extended resting time. Conversely, Zn plates resting in CCH only generate a stable and thin passivating Zn$(OH)_2$ layer (~500 nm). To quantify the Zn loss during aging in different hydrogels, the post-aging reversibility tests were performed (Figure S20).[48-49] The contrast in Zn retention between two hydrogel systems increases with time. The Zn plate in DICH suffers around 80% Zn loss after 96 h aging, while the one in CCH still retains 74.8 % reversible Zn (Figure 3f), suggesting that CCH effectively inhibits consecutive HER corrosion and preserves the Zn.

To explore Zn deposition behavior, we conducted chronoamperometry (CA) tests using a zinc symmetric cell (Figure S21). In comparison with DICH and PAm-AMPH, CCH reveals a more stable current density, indicative of a constrained 2D surface diffusion process.[50] Optical microscopy of the Zn anode visualizes that after a 30-min plating process, isolated clusters of dendrites formed on the Zn surface with DICH, while no evident protuberance is observed on the Zn plate in DICH (Figure S22). To gain insight into the micromorphology of the plated Zn, we examined the Zn surface through SEM after electrodepositing at 2 mA cm^{-2} for 15 h. Random and loose accumulation of flakes-like dendrites appeared on Zn in DICH and PAm-AMPH (**Figure 4**a-b, Figure S23a and S24). Conversely, the deposited Zn within CCH presented compact flakes with a hexagon shape (Figure 4c-d, Figure S23c), exposing the (002) crystal plane. Such uniform Zn nucleation endows Zn metal with a homogeneous dark grey surface on a macroscopic scale (inset digital photographs). On the stripping side (Figure 4e-f, Figure S23b and S23d), the Zn plate in DICH illustrates a mixed appearance composed of the original pristine part and uneven pits. In contrast, a relatively flat surface with uniform dimple distribution was attained in CCH (Figure 4g-h and S25).

The images collected by laser confocal scanning microscope (LSCM) were further studied to compare the surface roughness of the plated/stripped Zn in various hydrogels. As concluded in Figure 4i-l and Figure S23e-h, the values of the S_a (arithmetical mean height), S_z (maximum height), and S_{dr} (developed surface area ratio) of the plated Zn in CCH are 0.8, 10.5, and 0.5, respectively. These values are extremely lower than those observed for Zn in DICH (6.8, 47.3, 0.7). Similarly, the S_a, S_z, and S_{dr} values for the stripped Zn in CCH (2.7, 37.8, 0.6) are also lower than those in DICH (16.7, 96.2, 1.2). Hence, it is suggested that the Zn surface in CCH remains smoother during dynamic redox process than that in DICH.

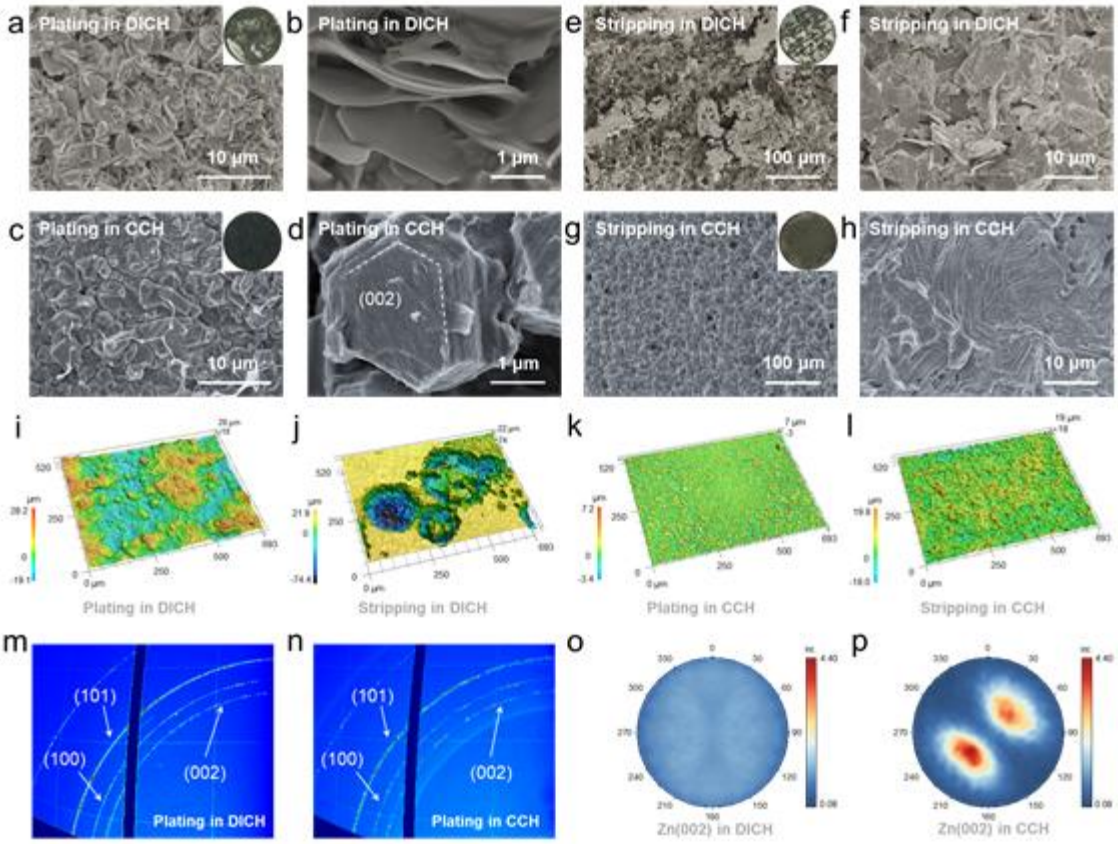

Figure 4. Characterizations of the Zn after plating and stripping. (a-d) SEM images of Zn plates after deposition (2 mA cm^{-2} for 15 h). (e-h) SEM images of Zn after stripping. Insets are corresponding digital photographs. LSCM images of Zn plates after plating and stripping in (i, j) DICH and (k, l) CCH. (m, n) GIWAXS patterns of Zn plates after deposition. (o, p) The (002) plane pole figures of the Zn deposits in DICH and CCH.

Additionally, the grazing-incidence wide-angle X-ray scattering (GIWAXS) pattern of the Zn plate after deposition in CCH reveals discrete diffraction spots in the ring plane (Figure 4m-n), as opposed to the continuous diffraction rings of the Zn plate in DICH. This illustrates that the precipitated Zn in DICH exhibits a polycrystalline structure with a random orientation.[51] To better justify the preferential orientation along the (002) plane, XRD patterns were presented after different plating times (Figure S26a-b). With increasing deposition time, the $I_{(002/101)}$ ratio of Zn in CCH continuously increases from the initial value of 0.35 to 0.85 after 15 h, whereas the nucleation in DICH results in a reduction of $I_{(002/101)}$.

The corresponding pole figures of the Zn plates after 15 h were collected (Figure 4o-p). Zn deposited with the assistance of CCH delivers a much stronger focused distribution along the (002) plane compared to (100) and (101) orientations (Figure S26c-f). However, Zn deposited in DICH displays a weak and dispersed intensity of the (002) plane. Possible reasons to the distinct nucleation behavior are include the differences in side reactions, interfacial adhesion strengths, and interfacial kinetics.[52] Hence, CCH with anti-HER property and solid Zn adhesion has enabled a Zn (002) texture during both plating and stripping processes.

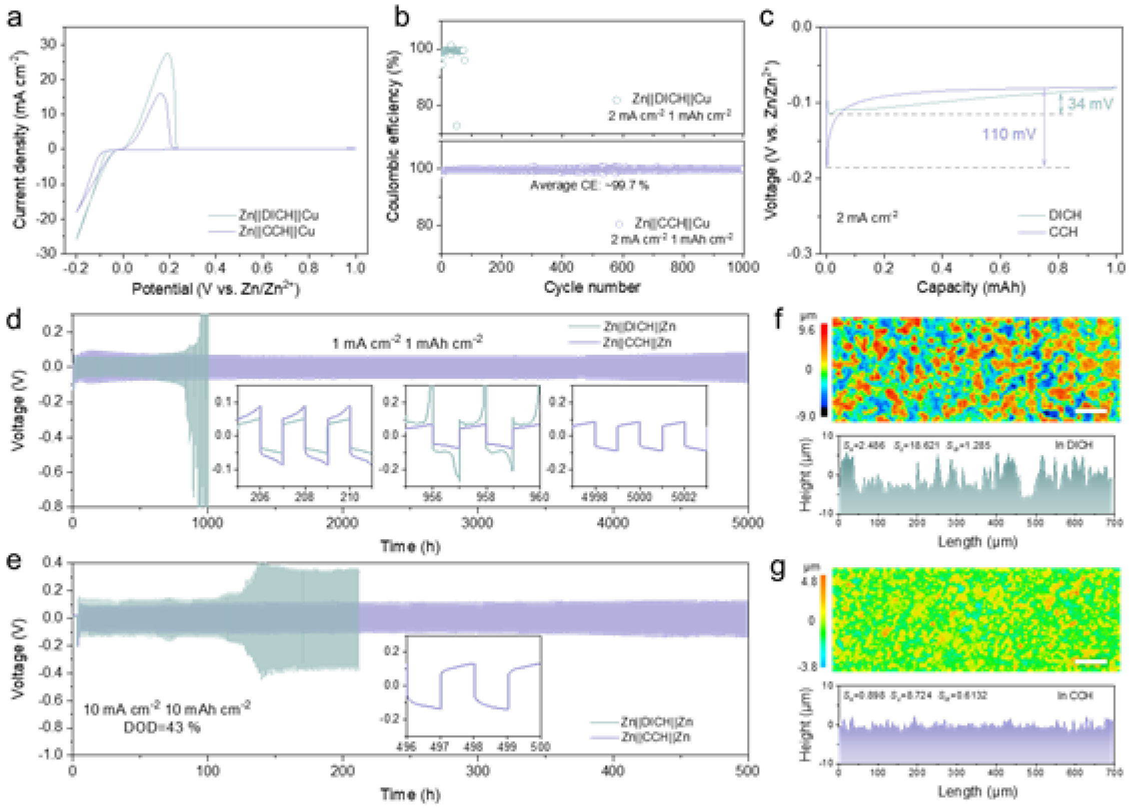

Figure 5. Stability of Zn anodes. (a) CV curves, (b) Coulombic efficiency tests, and (c) nucleation overpotentials of Zn||Cu half cells. Cycling performance of symmetric cells at (d) 1 mA cm^{-2}, 1 mAh cm^{-2} (Zn plate thickness: 100 μm), and (e) 10 mA cm^{-2}, 10 mAh cm^{-2} (Zn foil thickness: 20 μm). Insets are magnified voltage profiles. CLSM images and surface roughness of cycled Zn anodes in (f) DICH and (g) CCH (Scale bar: 50 μm).

To evaluate the optimized Zn growth in CCH electrolyte concerning the reversibility of Zn anode, Zn||Cu half cells were assembled with different hydrogels. The cyclic voltammetry (CV) curves reveal that Zn anodes in both CCH and DICH present apparent and distinct redox peaks (**Figure 5**a and Figure S27).[53] The decreased peak current density of the Zn dissolution process in CCH may be due to its lower ionic conductivity. The Coulombic efficiency (CE) at 2 mA cm^{-2} with a cut-off capacity of 1 mAh cm^{-2} was investigated as well (Figure 5b). In CCH, a steady CE with an average value of 99.7 % is consistently maintained over 1000 cycles. Contrariwise, the DICH cell fails within 100 cycles. The corresponding voltage profiles also justify the stable polarization of Zn plating/stripping in CCH (Figure S28a-b). While PAm-AMPH delivers a commendable average CE of 98.7 %, the corresponding polarization is quite large (Figure S28c-d). Notably, according to the initial cycle of CE test, CCH determines a higher overpotential for Zn nucleation and higher voltage separation compared to DICH (Figure S28e and Figure 5c), which accords with the CV results (Figure 5a). This enlarged nucleation overpotential is indicative of the formation of finely grained Zn nucleates with favorable crystallographic orientation, as supported by the SEM images (Figure S28f).[54] Aligning with the CA test, the strong interaction between hydrogel and Zn surface compels Zn^{2+} to nucleate at sites of initial adsorption without excess in-plane diffusion.

In the long-term cycling test of zinc symmetric cells, Zn||CCH||Zn exhibits stable voltage separation around 200 mV over 5000 h without short at 1 mA cm^{-2} for 1 mAh cm^{-2} (Figure 5d). This performance surpasses that of Zn||PAm-AMPH||Zn (~3800 h) and Zn||DICH||Zn (~800 h) (Figure S29). Upon elevating the current density to 10 mA cm^{-2} with a corresponding capacity of 10 mAh cm^{-2} at the depth of discharge (DOD) of 43 %, the Zn||CCH||Zn cell stably cycles for 500 h. In contrast, the Zn||DICH||Zn cell suffers serious voltage fluctuation due to the ZSH passivation and the emergence of dead Zn (Figure 5e). By employing thin Zn foil (10 μm) and increasing the DOD to ~85.4 %, the symmetric cell with CCH still shows remarkable lifespan around 140 h at current densities of 20 mA cm^{-2} for 10 mAh cm^{-2} (Figure S30).

According to the SEM images of the Zn plates after cycling at 1 mA cm^{-2} (Figure S31a-b), it is evident that CCH generates a more compact and homogeneous distribution of Zn, as opposed to the loose flakes coverage on Zn cycled in DICH. The corresponding LSCM images and surface roughness analysis (Figure 5f-g and Figure S31c-d) further certify the flat anode surface that has been maintained in CCH after long-term cycles (surface roughness parameters: S_a=0.9, S_z=8.7, S_{dr}=0.6 in CCH versus S_a=2.5, S_z=18.6, S_{dr}=1.3 in DICH). The ex-situ XRD patterns of Zn plates at different cycling times verify the preferred orientation along Zn (002) plane in CCH with the absence of ZSH (Figure S31e-f). Finally, the superiority of the CCH in enhancing the lifespan of Zn symmetric cells is summarized in Figure S32.

To demonstrate the practical utility of CCH electrolyte in AZIB, we constructed iodine cathodes using a mixture of activated carbon host and I_2 (Figure S33). CV profiles show one pair of redox peaks related to the typical two-electron reaction between I_2 and ZnI_2 (Figure S34a). When considering the rate performance, ZIB/CCH delivers noteworthy specific discharge capacities of 199, 184, 174, 162, and 147 mAh g^{-1} at current densities of 0.5, 1, 2, 4, and 10 C, respectively (**Figure 6**a). In contrast, ZIB/DICH only presents a capacity of 74 mAh g^{-1} at 10 C (Figure S34b). With regard to cycling performance (Figure 6b and Figure S35), ZIB/CCH gives an initial discharge capacity of 205 mAh g^{-1} at 2 C, surpassing that of ZIB/PAm-AMPH (191 mAh g^{-1}) and ZIB/DICH (178 mAh g^{-1}). Even after 2000 cycles, the capacity retains a value of 170 mAh g^{-1}. Conversely, ZIB/DICH maintains a discharge capacity of only 132 mAh g^{-1} after 500 cycles. When operating at a high current density of 10 C (Figure 6c), ZIB/CCH exhibits exceptional capacity retention with a low decay rate of 0.0076 ‰ per cycle after 22000 cycles, outperforming the most recently reported ZIBs (Figure S36). In contrast, the ZIB/DICH experienced failure at around 7000 cycles, marked by a sudden capacity drop. The failure of the cell with DICH is probably due to the irreversible loss of the iodine, and the side reactions at the Zn anode. This side reaction induces an increase in charge transfer resistance, primarily ascribed to the passivation by ZSH (Figure S37).

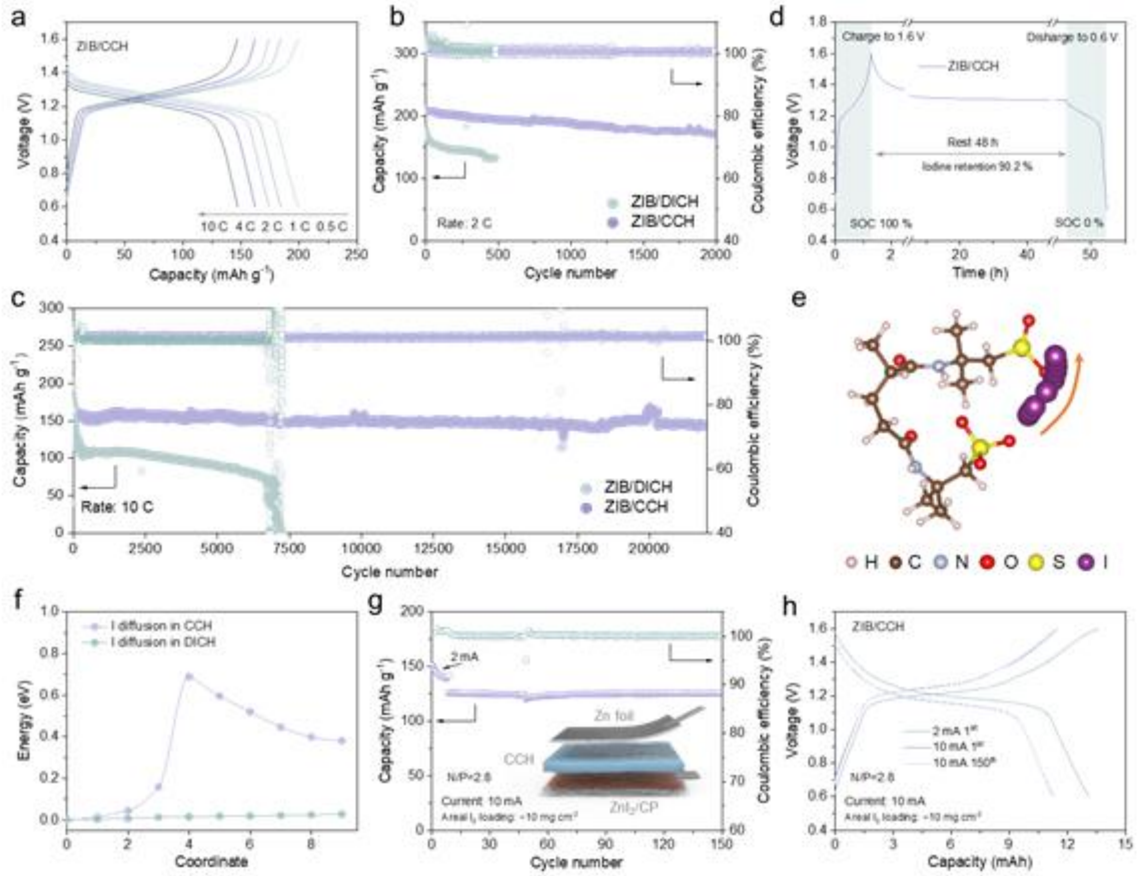

Figure 6. Zinc-iodine full cells. (a) Charge-discharge curves. (b, c) Cycling performance at 2 C and 10 C (1 C = 211 mA g^{-1}, based on mass of iodine). (d) Voltage-time profile of the cell with CCH in self-discharge test (Charge capacity: 182.4 mAh cm^{-2}, discharge capacity: 164.5 mAh cm^{-2}). (e) Optimized structure of iodine ion diffusion in CCH, and (f) corresponding energy profiles. (g) Cycling performance of the zinc-iodine pouch cell with CCH (inset is the schematic of the cell) and (h) the corresponding voltage profiles.

In the self-discharge assessment, the iodine retention rose from 44.0 % in DICH to 90.2 % in CCH (Figure 6d and Figure S38). Cross-sectional SEM images of ZIB also clarify the relieved penetration of iodine species in CCH (Figure S39). This notable enhancement in iodine retention in ZIB/CCH should be related to the elimination of polyiodides transport within the hydrogel. The isolated iodine ion diffusion barrier in CCH is around 0.7 eV, a considerably higher value compared to the 0.02 eV barrier observed in DICH (Figure 6e-f and Figure S40). This underscores the ability of the $–SO_3^-$ on CCH in hindering the shuttle effect by exerting an electrostatic repulsion on negatively charged iodine species.[55-56]

Furthermore, we fabricated a Zn-I_2 pouch cell (3×3 cm) with a low N/P ratio of around 2.8. ZnI_2 was employed as the initial active material in cathode with an areal I_2 loading of approximately 10 mg cm^{-2} (Figure S41). The ZIB/CCH pouch cell delivers a capacity of 125 mAh g^{-1} after 150 cycles at 10 mA (Figure 6g-h), displaying a better iodine retention compared with the pouch cell with DICH (Figure S42). No obvious polyiodides shuttling or anode corrosion has been observed (Figure S43). This highlights the potential feasibility of applying CCH in quasi-solid batteries with high durability.

3. Conclusion

A cation-conduction dominated hydrogel with an improved Zn transference number of 0.81 has been developed by the means of an anions-tethered strategy. Central to this design are the functional groups of the polymers chain. The covalently bonded $-SO_3^-$ groups on hydrogel chains maintain the concentration of anions near the anode surface throughout the Zn plating/stripping process. This effect, in turn, streamlines the formation of a flat and dense Zn anode surface. Additionally, the presence of zincophilic $-SO_3^-$ in the hydrogel optimizes the solvation structure of Zn^{2+}, while the dissociation of Zn^{2+} is refined by amide groups, which facilitates a smooth ion migration and propels Zn^{2+} desolvation. The strong hydrogen bond with H_2O induced by the functional groups of the hydrogel framework suppresses the HER reaction and parasite passivation. The Zn symmetric cell with CCH presents over 5000 h lifespan at 1 mA cm^{-2}, and over 500 h at high DOD of 43 % under 10 mA cm^{-2}. Another important effect by this CCH electrolyte design is, the CCH electrolyte effectively alleviates the shuttling of polyiodides through an electrostatic repulsion mechanism, thereby prolonging the battery lifespan (over 22000 cycles at 10 C) and enhancing the iodine utilization. This work may mark a leap forward in the pursuit of reliable aqueous energy storage solutions.

Keywords: cation-conduction, anion-tethered hydrogel, Zn dendrites, polyiodides shuttle effect, aqueous zinc-iodine battery

Declaration of Competing Interest

The authors declare no conflict of interest.

Author Contributions

P.Y. and H.J.F. supervised the project. J.-L.Y. and P.Y. conceived the idea. J.-L.Y., T.X., and J.L. carried out the experiments, collected and analyzed the experimental data. T.X. and Z.Y. performed the simulations, K.L., P.Y., and H.J.F. provided helpful advice on manuscript preparation. J.-L.Y., P.Y. and H.J.F. wrote the paper. All authors participated in discussions of the results.

Acknowledgments

P.Y. acknowledges the National Natural Science Foundation of China (22209124), the Fundamental Research Funds for the Central Universities (2042023kf0115) and startup funding of Wuhan University. H.J.F. acknowledges financial support from the Singapore Ministry of Education by Tier 2 (MOE-T2EP50121-0006). J.-L.Y. is thankful for the financial support from the China Scholarship Council (No. 202006210070). The authors appreciate the Supercomputing Center of Wuhan University for numerical calculations supporting. J.-L.Y and T.X. contributed equally to this work.

Received: ((will be filled in by the editorial staff))
Revised: ((will be filled in by the editorial staff))
Published online: ((will be filled in by the editorial staff))

References

[1] Q. Yang, X. Li, Z. Chen, Z. Huang, C. Zhi, *Acc. Mater. Res.* **2022**, *3*, 78.

[2] K. Xu, X. Zheng, R. Luo, J. Sun, Y. Ma, N. Chen, M. Wang, L. Song, Q. Zhao, W. Chen, *Mater. Today Energy* **2023**, *34*, 101284.

[3] S. Wu, Z. Hu, P. He, L. Ren, J. Huang, J. Luo, *eScience* **2023**, *3*, 100120.

[4] D. Lin, Y. Li, *Adv. Mater.* **2022**, *34*, 2108856.

[5] M. Liu, Q. Chen, X. Cao, D. Tan, J. Ma, J. Zhang, *J. Am. Chem. Soc.* **2022**, *144*, 21683.

[6] J. Ma, M. Wang, H. Zhang, L. Fu, W. Zhang, B. Song, S. Lu, Q. Chen, K. Lu, *Mater. Today Energy* **2022**, *30*, 101146.

[7] H. Chen, X. Li, K. Fang, H. Wang, J. Ning, Y. Hu, *Adv. Energy Mater.* **2023**, *13*, 2302187.

[8] P. Bai, J. Li, F. R. Brushett, M. Z. Bazant, *Energy Environ. Sci.* **2016**, *9*, 3221.

[9] N. Meng, Y. Ye, Z. Yang, H. Li, F. Lian, *Adv. Funct. Mater.* **2023**, *33*, 2305072.

[10] T. Zhu, H. Sternlicht, Y. Ha, C. Fang, D. Liu, B. H. Savitzky, X. Zhao, Y. Lu, Y. Fu, C. Ophus, C. Zhu, W. Yang, A. M. Minor, G. Liu, *Nat. Energy* **2023**, *8*, 129.

[11] P. Zou, Y. Sui, H. Zhan, C. Wang, H. L. Xin, H. M. Cheng, F. Kang, C. Yang, *Chem. Rev.* **2021**, *121*, 5986.

[12] Y. He, C. Wang, P. Zou, R. Lin, E. Hu, H. L. Xin, *Angew. Chem. Int. Ed.* **2023**, *62*, e202308309.

[13] J.-L. Yang, L. Liu, Z. Yu, P. Chen, J. Li, P. A. Dananjaya, E. K. Koh, W. S. Lew, K. Liu, P. Yang, H. J. Fan, *ACS Energy Lett.* **2023**, *8*, 2042.

[14] L. Li, S.-F. Jia, M.-H. Cao, Y.-Q. Ji, H.-W. Qiu, D. Zhang, *Rare Metals* **2024**, *43*, 20.

[15] Y. Yang, H. Hua, Z. Lv, W. Meng, M. Zhang, H. Li, P. Lin, J. Yang, G. Chen, Y. Kang, Z. Wen, J. Zhao, C. C. Li, *ACS Energy Lett.* **2023**, *8*, 1959.

[16] M. Qiu, P. Sun, Y. Wang, L. Ma, C. Zhi, W. Mai, *Angew. Chem. Int. Ed.* **2022**, *61*, e202210979.

[17] Y. Cui, Q. Zhao, X. Wu, Z. Wang, R. Qin, Y. Wang, M. Liu, Y. Song, G. Qian, Z. Song, L. Yang, F. Pan, *Energy Storage Mater.* **2020**, *27*, 1.

[18] H. Xia, G. Xu, X. Cao, C. Miao, H. Zhang, P. Chen, Y. Zhou, W. Zhang, Z. Sun, *Adv. Mater.* **2023**, *35*, 2301996.

[19] S. Chen, Y. Ying, L. Ma, D. Zhu, H. Huang, L. Song, C. Zhi, *Nat. Commun.* **2023**, *14*, 2925.

[20] F. Wang, J. Zhang, H. Lu, H. Zhu, Z. Chen, L. Wang, J. Yu, C. You, W. Li, J. Song, Z. Weng, C. Yang, Q. H. Yang, *Nat. Commun.* **2023**, *14*, 4211.

[21] H. Lu, J. Hu, X. Wei, K. Zhang, X. Xiao, J. Zhao, Q. Hu, J. Yu, G. Zhou, B. Xu, *Nat. Commun.* **2023**, *14*, 4435.

[22] Z. Chen, T. Wang, Y. Hou, Y. Wang, Z. Huang, H. Cui, J. Fan, Z. Pei, C. Zhi, *Adv. Mater.* **2022**, *34*, 2207682.

[23] M. J. C. Plancha, C. M. Rangel, C. A. C. de Sequeira, *J. Solid State Electrochem.* **2012**, *16*, 665.

[24] P. Yang, J. L. Yang, K. Liu, H. J. Fan, *ACS Nano* **2022**, *16*, 15528.

[25] S. Zhao, Y. Zuo, T. Liu, S. Zhai, Y. Dai, Z. Guo, Y. Wang, Q. He, L. Xia, C. Zhi, J. Bae, K. Wang, M. Ni, *Adv. Energy Mater.* **2021**, *11*, 2101749.

[26] J. L. Yang, J. Li, J. W. Zhao, K. Liu, P. Yang, H. J. Fan, *Adv. Mater.* **2022**, *34*, 2202382.

[27] Z. Zhuang, Z. Yu, J. Yang, L. Chen, T. Xiao, R. Fu, Z. Huang, K. Liu, P. Yang, *Energy Storage Mater.* **2024**, *65*, 103136.

[28] T. Qiu, T. Wang, W. Tang, Y. Li, Y. Li, X. Lang, Q. Jiang, H. Tan, *Angew. Chem. Int. Ed.* **2023**, *62*, e202312020.

[29] J. Cong, X. Shen, Z. Wen, X. Wang, L. Peng, J. Zeng, J. Zhao, *Energy Storage Mater.* **2021**, *35*, 586.

[30] J. L. Yang, Z. Yu, J. Wu, J. Li, L. Chen, T. Xiao, T. Xiao, D. Q. Cai, K. Liu, P. Yang, H. J. Fan, *Adv. Mater.* **2023**, *35*, 2306531.

[31] Q. Liu, Z. Yu, Q. Zhuang, J. K. Kim, F. Kang, B. Zhang, *Adv. Mater.* **2023**, *35*, 2300498.

[32] Y. Qin, H. Li, C. Han, F. Mo, X. Wang, *Adv. Mater.* **2022**, *34*, 2207118.

[33] Y. Wang, Q. Li, H. Hong, S. Yang, R. Zhang, X. Wang, X. Jin, B. Xiong, S. Bai, C. Zhi, *Nat. Commun.* **2023**, *14*, 3890.

[34] D. Wang, D. Lv, H. Peng, C. Wang, H. Liu, J. Yang, Y. Qian, *Angew. Chem. Int. Ed.* **2023**, *62*, e202310290.

[35] H. Yu, D. Chen, X. Ni, P. Qing, C. Yan, W. Wei, J. Ma, X. Ji, Y. Chen, L. Chen, *Energy Environ. Sci.* **2023**, *16*, 2684.

[36] C. Wang, X. Zeng, J. Qu, J. M. Cairney, Q. Meng, P. J. Cullen, Z. Pei, *Matter* **2023**, *6*, 3993.

[37] Y. Zhang, Z. Liu, X. Li, L. Fan, Y. Shuai, N. Zhang, *Adv. Energy Mater.* **2023**, *13*, 2302126.

[38] W. Xu, J. Li, X. Liao, L. Zhang, X. Zhang, C. Liu, K. Amine, K. Zhao, J. Lu, *J. Am. Chem. Soc.* **2023**, *145*, 22456.

[39] W. Zhang, F. Guo, H. Mi, Z. S. Wu, C. Ji, C. Yang, J. Qiu, *Adv. Energy Mater.* **2022**, *12*, 2202219.

[40] H. Li, Y. Ren, Y. Zhu, J. Tian, X. Sun, C. Sheng, P. He, S. Guo, H. Zhou, *Angew. Chem. Int. Ed.* **2023**, *62*, e202310143.

[41] M. Jiao, L. Dai, H. R. Ren, M. Zhang, X. Xiao, B. Wang, J. Yang, B. Liu, G. Zhou, H. M. Cheng, *Angew. Chem. Int. Ed.* **2023**, *62*, e202301114.

[42] Z. Miao, F. Zhang, H. Zhao, M. Du, H. Li, H. Jiang, W. Li, Y. Sang, H. Liu, S. Wang, *Adv. Funct. Mater.* **2022**, *32*, 2111635.

[43] S. Chen, D. Ji, Q. Chen, J. Ma, S. Hou, J. Zhang, *Nat. Commun.* **2023**, *14*, 3526.

[44] G. Guo, C. Ji, H. Mi, C. Yang, M. Li, C. Sun, L. Sun, *Adv. Funct. Mater.* **2023**, *33*, 2308405.

[45] W. Wang, S. Chen, X. Liao, R. Huang, F. Wang, J. Chen, Y. Wang, F. Wang, H. Wang, *Nat. Commun.* **2023**, *14*, 5443.

[46] P. J. Flory, *J. Chem. Phys.* **1941**, *9*, 660.

[47] J. Wei, P. Zhang, T. Shen, Y. Liu, T. Dai, Z. Tie, Z. Jin, *ACS Energy Lett.* **2022**, *8*, 762.

[48] S. D. Pu, B. Hu, Z. Li, Y. Yuan, C. Gong, Z. Ning, C. Chau, S. Yang, S. Zhang, L. Pi, Y. T. Tang, J. Yue, T. J. Marrow, X. Gao, P. G. Bruce, A. W. Robertson, *Joule* **2023**, *7*, 366.

[49] Z. Cai, J. Wang, Y. Sun, *eScience* **2023**, *3*, 100093.

[50] Z. Zhao, J. Zhao, Z. Hu, J. Li, J. Li, Y. Zhang, C. Wang, G. Cui, *Energy Environ. Sci.* **2019**, *12*, 1938.

[51] Z. Zhao, R. Wang, C. Peng, W. Chen, T. Wu, B. Hu, W. Weng, Y. Yao, J. Zeng, Z. Chen, P. Liu, Y. Liu, G. Li, J. Guo, H. Lu, Z. Guo, *Nat. Commun.* **2021**, *12*, 6606.

[52] J. Wang, B. Zhang, Z. Cai, R. Zhan, W. Wang, L. Fu, M. Wan, R. Xiao, Y. Ou, L. Wang, J. Jiang, Z. W. Seh, H. Li, Y. Sun, *Sci. Bull.* **2022**, *67*, 716.

[53] X. Wang, Y. Ying, X. Li, S. Chen, G. Gao, H. Huang, L. Ma, *Energy Environ. Sci.* **2023**, *16*, 4572.

[54] M. Kim, J. Lee, Y. Kim, Y. Park, H. Kim, J. W. Choi, *J. Am. Chem. Soc.* **2023**, *145*, 15776.

[55] P. Lin, G. Chen, Y. Kang, M. Zhang, J. Yang, Z. Lv, Y. Yang, J. Zhao, *ACS Nano* **2023**, *17*, 15492.

[56] L. Zhang, J. Huang, H. Guo, L. Ge, Z. Tian, M. Zhang, J. Wang, G. He, T. Liu, J. Hofkens, D. J. L. Brett, F. Lai, *Adv. Energy Mater.* **2023**, *13*, 2203790.

Table of Content Entry

A cation-conduction conductive hydrogel has been engineered based on the anion-tethered strategy, distinguished by synergistic solvation effect, finely adjusted zinc nucleation properties, and the fortitude of iodine reactions, all with the specific intent of bolstering the durability and reliability of Zn-iodine batteries. This work is believed to push the progress of durable quasi-solid conversion-type aqueous batteries.